energies

MDPI

Article

Sub-Sonic Linear Synchronous Motors Using Superconducting Magnets for the Hyperloop

Su Y. Choi, Chang Y. Lee, Jung M. Jo, Jae H. Choe, Ye Jun Oh, Kwan S. Lee and Jung Y. Lim *

New Transportation Innovative Research Center, Korea Railroad Research Institute, Uiwang-si, Gyeonggi-do 16105, Korea; suchoi@krri.re.kr (S.Y.C.); cylee@krri.re.kr (C.Y.L.); jmjo@krri.re.kr (J.M.J.); cjh@krri.re.kr (J.H.C.); yoh@krri.re.kr (Y.J.O.); kslee@krri.re.kr (K.S.L.)

* Correspondence: jlim@krri.re.kr

Received: 6 November 2019; Accepted: 1 December 2019; Published: 4 December 2019

Abstract: Sub-sonic linear synchronous motors (LSMs) with high-temperature superconducting (HTS) magnets, which aim to accelerate to a velocity of 1200 km/h in the near-vacuum tubes of 0.001 atm for the Hyperloop, are newly introduced in this paper. By the virtue of the combination of LSMs and electrodynamic suspensions (EDSs) with HTS magnets, a large air-gap of 24 cm, low magnetic resistance forces of below 2 kN, and the efficient as well as practical design of propulsion power supply systems of around 10 MVA could be guaranteed at a sub-sonic velocity. The characteristics of the proposed LSMs with HTS magnets, in addition, are widely analyzed with theories and simulation results. Optimal design methods for LSMs and inverters, which account for more than half of the total construction cost, are introduced with design guidelines and examples for the commercialization version of the Hyperloop. At the end of the paper, in order to verify the proposed design models of the sub-sonic LSMs, two different test-beds—i.e., 6 m long static and 20 m long dynamic propulsion test-beds—are fabricated, and it is found that the experimental results are well matched with proposed design models as well as simulation results; therefore, the design methods constitute guidelines for the design of sub-sonic LSMs for the Hyperloop.

Keywords: Hyperloop; magnetic levitation train (Maglev); superconducting magnet (SCM); linear synchronous motor (LSM); propulsion power supply system (PPSS)

1. Introduction

The Hyperloop, which aims to accelerate to the sub-sonic velocity of 1200 km/h in near-vacuum tubes of 0.001 atm with magnetic levitation and propulsion systems, is an attractive candidate for the next-generation transportation [1,2]. This is because it can be free from the main problems of both conventional high-speed wheel on rail trains (WRTs) and magnetic levitation trains (Maglevs) to enhance its operating velocity. The main barriers to WRTs increasing their velocity are 1) an insufficient friction force between the wheels and rails for high acceleration and deceleration, and 2) the lack of power transfer methods from infrastructure to WRTs for on-board traction motors over 500 km/h due to the spark issues of pantographs [3,4]. To solve these problems, Transrapid [5] and JR-Maglev [6–9] systems have been developed in Germany and Japan, respectively; however, they still suffer two main problems: 1) massive infrastructure costs and 2) high aerodynamic resistance force at high operating speeds, resulting in massive electric power consumption to maintain operating velocity. After the alpha-paper on the Hyperloop [10] made by Space X was widely released in 2013, the Hyperloop has been suddenly in the public eye for the last several years as an alternative to replace Maglevs; however, similar concepts to the Hyperloop had already been introduced by Swissmetro, Switzerland since the 1990s [11] and developed in the Korea Railroad Research Institute (KRRI), South Korea since 2009 [12,13]. In the recently-created industry of the Hyperloop, there are dozens of venture companies

around the world, and two of them are becoming widely-known companies, Virgin Hyperloop One [14] and Hyperloop Transportation Technologies [15], which have performed partial operating tests [16,17]. Many of these companies, at the same time, have adopted linear induction motors (LIMs) with electrodynamic suspension (EDS) using on-board permanent magnets for propulsion, guidance and levitation. This is mainly because the system configuration, which does not require any sub-systems for the synchronization between fields and armatures, is simpler and easier than that of linear synchronous motors (LSMs) [18]. With the combination of the LIMs and EDS, on the other hand, technical issues—i.e., small air-gaps, low efficiencies, low-positioning precisions of LIMs [19], and the high magnetic resistance forces of the EDS—need to be solved with a technical breakthrough to increase the operating velocity of the Hyperloop to a sub-sonic velocity. At the same time, due to the technical issues of the LIMs and EDS for high-speed applications, there have been several research teams [20–26] who have adopted LSMs with high-temperature superconducting (HTS) magnets for high-speed transportation; however, most of them could not suggest general design guidelines covering magnetic propulsion systems. Moreover, they only conducted design and feasibility studies based on finite element method (FEM) simulations without any static and dynamic experiments due to the complex system configuration and cost issues.

In this paper, sub-sonic LSMs with HTS magnets for the Hyperloop are newly introduced and widely analyzed with theories, simulations, and experimental results conducted in static and dynamic propulsion test-beds. In detail, the characteristics of the proposed sub-sonic LSMs are introduced from scratch, and we suggest design guidelines with a design example for the commercialization version of the Hyperloop. In order to verify the proposed design of the sub-sonic LSMs, two different test-beds—i.e., 6 m long static and 20 m long dynamic propulsion test-beds—were fabricated, and the experimental results are well matched with the proposed design models and simulation results. As a result, it can be said that a large air-gap of 24 cm, low magnetic resistance forces of below 2 kN, and the efficient and practical design of propulsion power supply systems of around 10 MVA could be guaranteed even at a sub-sonic velocity by virtue of the combination of the LSMs and EDS with HTS magnets.

2. Sub-Sonic Linear Synchronous Motors with HTS Magnets

2.1. Overviews

In general, linear synchronous motor propulsion systems (LSMPSs) include two sub-systems: one is the LSM and the other is the propulsion power supply system (PPSS). As shown in Figure 1, the LSMs are composed of DC fields and multi-phase armatures while the PPSSs consist of pulse width modulation (PWM) converters, variable-voltage variable-frequency (VVVF) inverters, section switches, and sub-sonic light detection and ranging (LiDAR) sensors for the synchronization between the on-board DC fields and armatures.

In fact, there are two choices for system engineers: to adopt or eliminate the armatures between arrival and departure in the proposed LSMPSs. This is because EDSs with HTS magnets for levitation result in low magnetic resistance forces of below 2 kN; therefore, the pods are outside of the departure region in which armatures are not installed, and so pods can be continuously operated as there is a small decrease in velocity. However, at the same time, the pods are completely out of the control of the control tower, in the same way as a bullet. On the other hand, when armatures are installed for the entire region, the pods are always under control, but the construction cost will be further increased. Depending on the installation location of the armature between the pod and ground, there are two types of LSMs: short and long-armature LSMs. Short-armature LSMs can be free from the complexities of PPSSs [19]. At the same time, on the other hand, pods should not only have an on-board PPSS, which increases the weight of pods a great deal, but also contact-power transfer systems from the ground infrastructure to pods. In fact, the contact—i.e., pantograph—power transfer systems have a speed limit below 600 km/h [20] due to the arc problem. On the other hand, contactless-power

transfers—i.e., capacitive and inductive power transfer—could be one of the strong candidates to mitigate the problem.

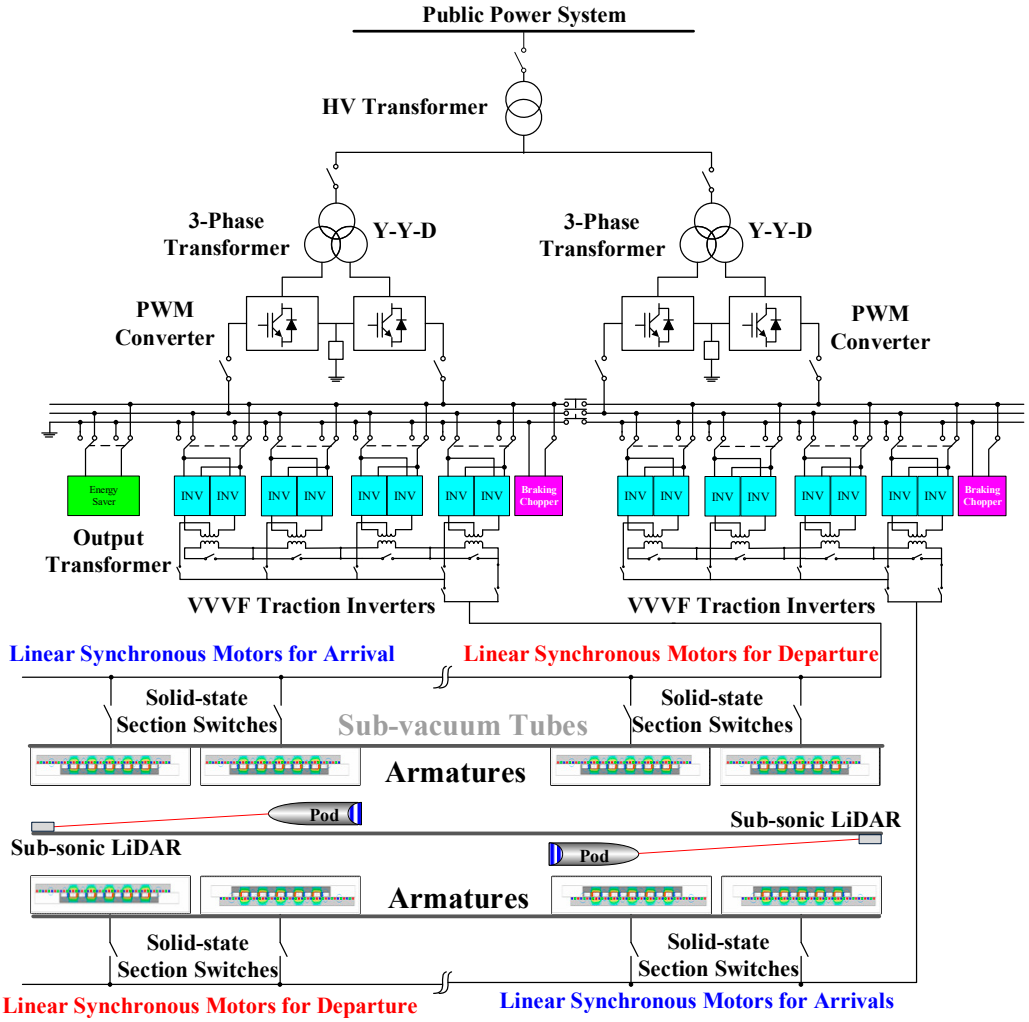

Figure 1. The overall configuration of sub-sonic linear synchronous motor propulsion systems (LSMPSs) for a Hyperloop adopting long-armature linear synchronous motors (LSMs). HV: high voltage; PWM: pulse width modulation; VVVF: variable-voltage variable-frequency.

Therefore, in order to achieve a sub-sonic velocity for the Hyperloop, the long-armature LSMs, which have double-sided long-armature windings in the sub-vacuum tubes, and DC fields on pods, as shown in Figure 2a, would be the best choice at the moment. This is because the required power of the PPSSs can be directly supplied from a public power system regardless of its operating velocity. With the concept of long-armature LSMs, high-temperature superconducting (HTS) magnets installed on pods are adopted for the proposed sub-sonic LSM as the DC fields to maximize the air-gap between pods and armatures and to achieve the optimal design of LSMs and PPSS for the Hyperloop [20,21].

In addition, among the various types of LSMs with HTS magnets, the three-phase, double-layer, and concentrated winding method are adopted for the highly efficient design of armatures [22] and their mass production in the future, while air-cores are chosen to avoid magnetic saturation and unwanted forces on pods due to the high magnetic fluxes generated by HTS magnets [20,21], as shown in Figure 2b.

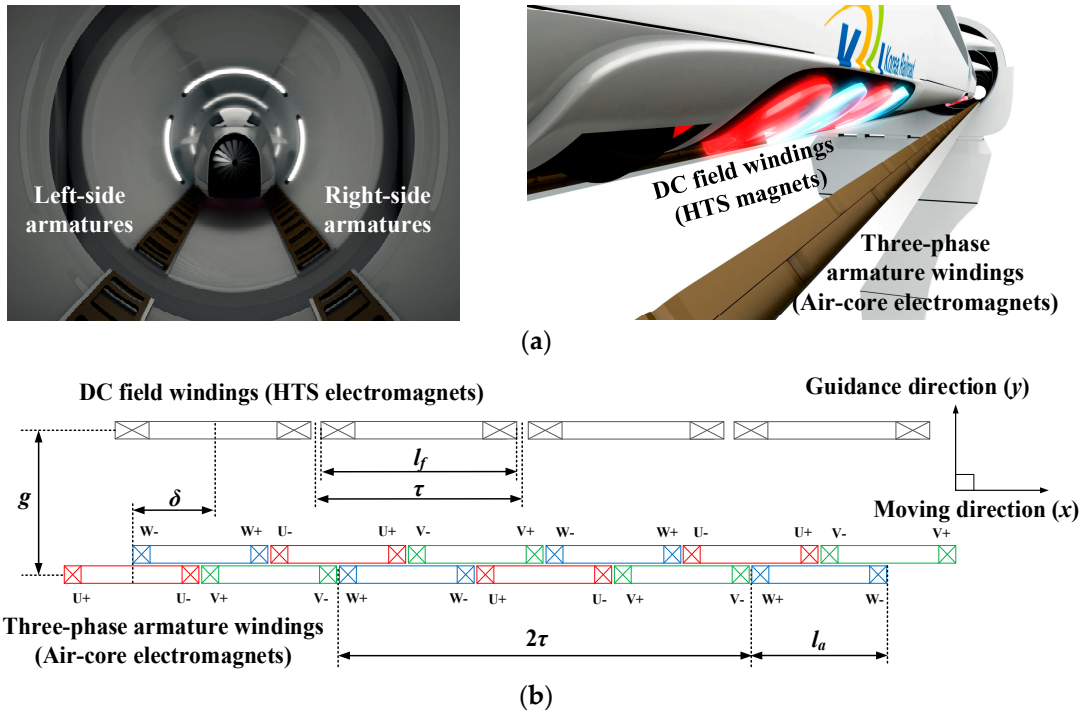

Figure 2. The configuration of the proposed Hyperloop with sub-sonic LSMs. (**a**) Front and bird's-eye views; (**b**) simplified one-sided drawing adopting a four pole–one module high-temperature superconducting (HTS) magnet and air-core electromagnets in the left-side.

2.2. *Analysis of Linear Synchronous Motors with HTS Magnets*

When three-phase armature windings are perfectly aligned and synchronized with DC field windings—i.e., with a power angle of 90°—each phase of the armature windings generates the maximum thrust forces, with the second harmonics of its operating frequency fs on pods with a 120° phase shift, while the sum of the thrust forces results in a total force including its sixth harmonics, as shown in Figure 3a. At the same time, each phase of the armature windings evenly generates guidance forces, and their sum then goes to zero with the same sixth harmonics, as shown in Figure 3b.

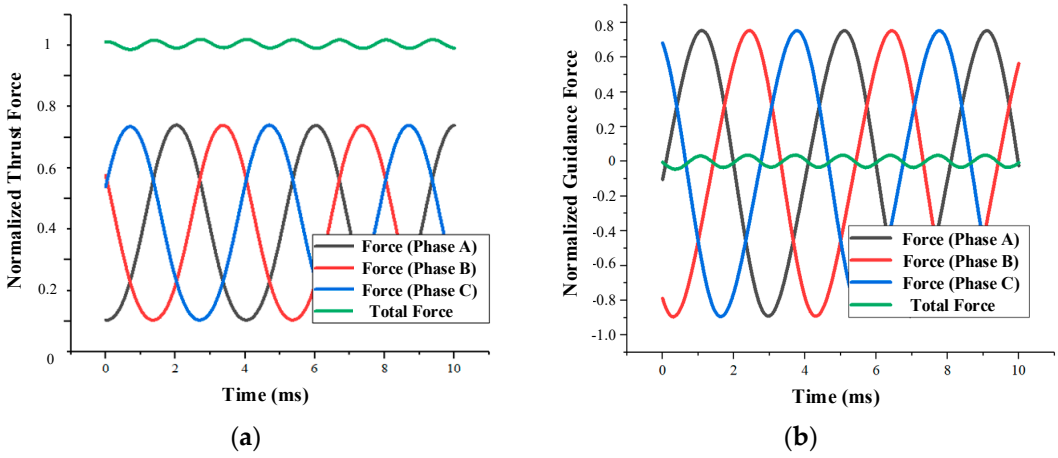

Figure 3. The 3D simulation results (Infolytica MagNet) of normalized thrust and guidance forces when the armature windings are perfectly synchronized with DC field windings at a sub-sonic velocity: (**a**) thrust forces; (**b**) guidance forces.

Simply, assuming $l_f = l_a$ and $w_f = w_a$, the generated maximum forces $F_{\max}$ on pods can be described as follows:

$$F_{\max} = c\mu_0 m_a p_e N_a I_a N_f I_f \frac{w_f l_f}{\tau} e^{-\alpha g} \quad (1)$$

where c is the design constant including winding and geometric factors, μ_0 is the permeability of free space, m_a is the number of phases, p_e is the number of field pole pairs, τ is the pole pitch, α is the gap constant, g is the air-gap, l_f and w_f are the effective length and width of field windings, N_a and N_f are the number of coil turns per phase for armature and DC field windings, and I_a and I_f are the current of armature and DC field windings, respectively. In Figure 4, l_a and w_a show the effective length and width of armature windings, and g_c is the center difference between field and armature windings.

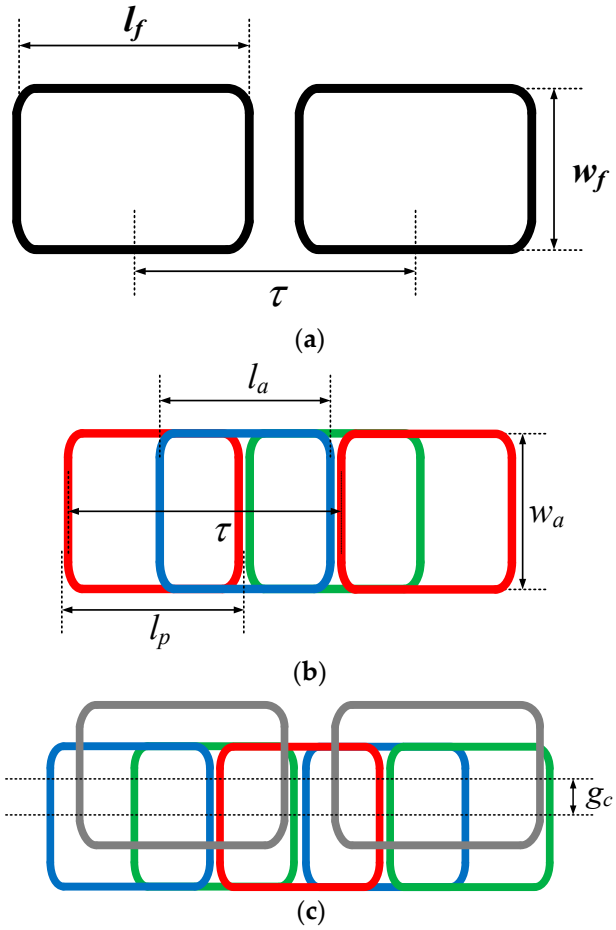

Figure 4. Definition of the dimensions of the proposed LSMs: (**a**) HTS magnets (two poles); (**b**) three-phase armature windings with a pitch l_p of $2\tau/3$; (**c**) HTS magnet on the armature winding.

From Equation (1), the thrust force F_t and guidance force F_g can be obtained as follows:

$$F_t = F_{max} \sin \delta \quad (2a)$$

$$F_g = -F_{max} \cos \delta \quad (2b)$$

where δ is the power angle. In order to achieve the most efficient operation of the proposed LSMs, the largest F_t and the smallest F_g can be guaranteed when δ is maintained near 90°. For this issue, the real-time location measurement of pods with high-resolutions is a significant technological requirement; therefore, sub-sonic LiDAR sensors are newly adopted for the Hyperloop using the proposed LSMs.

In the case when δ increases from 90°, the thrust forces gradually decrease while repulsive forces significantly increase, as shown in Figure 5. On the other hand, when δ decreases from 90°, thrust forces decrease as attractive forces significantly increase. Therefore, in terms of the dynamic stability of pods, δ should be controlled above 90° to avoid unwanted physical contacts between pods and armatures at a sub-sonic velocity, as these could lead to massive accidents. As shown in Figure 6, each phase of armatures with the DC fields can be simplified as the ideal voltage source, controlled voltage source, controlled current source, inductor and resistance as follows:

$$\boldsymbol{V}_T = \boldsymbol{I}_a \left(R_a + j\omega_s L_a\right) + \boldsymbol{E}_i \tag{3a}$$

$$R_a = N_p \, R_{pa} \tag{3b}$$

$$L_a = N_p \, L_{pa} \tag{3c}$$

$$E_i = c_i \, p_e \, N_a \, \phi_a \, v_s \tag{3d}$$

where $\boldsymbol{V_T}$ is the stator voltage for each phase, R_a and L_a are the total resistance and inductance of armature windings for each phase, respectively, N_p is the number of armature poles for each phase, R_{pa} and L_{pa} are the resistance and inductance of each pole of armature windings, $\boldsymbol{E_i}$ is the induced voltage generated by moving pods with DC fields on each phase of armature windings, c_i is the induced voltage constant, vs. is the speed of pods, and ϕ_a is the magnetic flux passing through the armature windings.

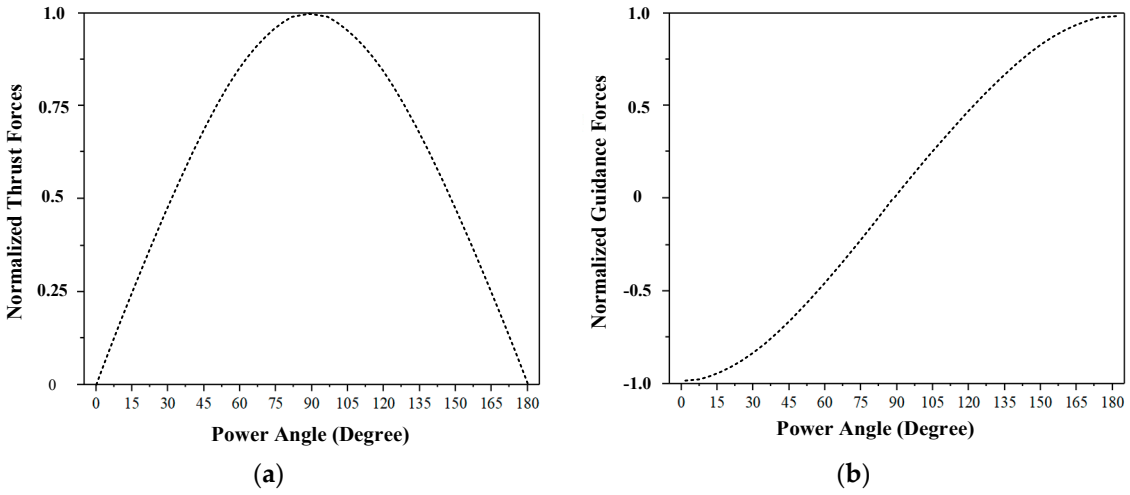

Figure 5. The 3D simulation results of averaged total thrust and guidance forces along with variable power angles in the case when $g > \tau$, 3; here, lift forces are zero with a g_c of 0: (**a**) normalized thrust forces; (**b**) normalized guidance forces.

At the same time, the mechanical force F_m, which is the same as thrust force F_t, total resistance forces F_r, and effective thrust forces F_f are included in the simplified equivalent circuits and can be summarized as follows:

$$F_r = F_a + F_d + F_i \cong F_d \tag{4a}$$

$$F_f = F_m - F_r = m_s a_s \tag{4b}$$

where F_a is the aerodynamic resistance force, F_d is the electrodynamic resistance force, F_i is the incline resistance force, and m_s and a_s are the mass and acceleration of pods. In general, for the LSM design of the Hyperloop, F_r can be simplified as F_m because the Hyperloop is supposed to be operated in flat sub-vacuum tubes resulting in the significant decrease of F_a and F_i. Due to conductive and ferromagnetic materials being used in guideways and tubes as well as electrodynamic levitations,

on the other hand, finding the optimal design approach to reducing the electrodynamic resistance force should be one of the main research issues for efficient sub-sonic linear motors.

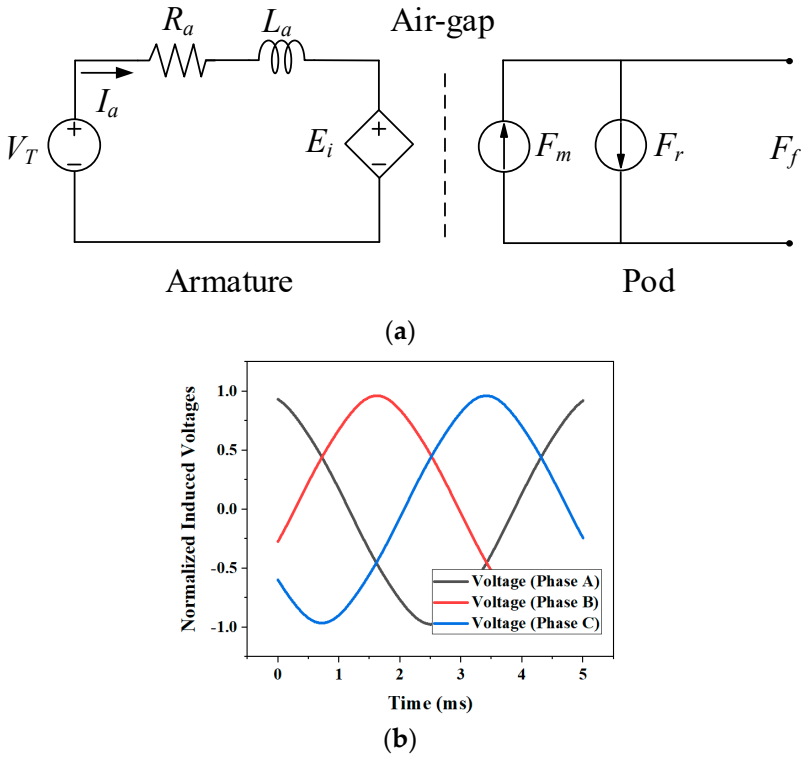

Figure 6. (**a**) Simplified equivalent circuit of LSMs and (**b**) simulation result of induced voltages for each phase under the no-load condition.

Next, the electrical power P_e and mechanical power P_m can be simply defined as follows:

$$P_e = m_a E_i I_a \cos(\gamma) \tag{5a}$$

$$P_m = F_m vs. \tag{5b}$$

$$P_e = P_m \tag{5c}$$

where γ is the phase difference between the induced voltage and armature phase current.

The electrical parameters of LSMs can be summarized in the phase diagram, as shown in Figure 7, while power equations can be also obtained from the phase diagram as follows:

$$P = m_a V_T I_a \cos\theta \tag{6a}$$

$$Q = m_a V_T I_a \sin\theta \tag{6b}$$

$$S = m_a V_T I_a \tag{6c}$$

where P is the active power including electrical DC and AC losses and mechanical propulsion power, Q is the reactive power mainly coming from the inductance of armature windings, and S is the complex power, which is equal to the capacity of LSMs as well as inverters.

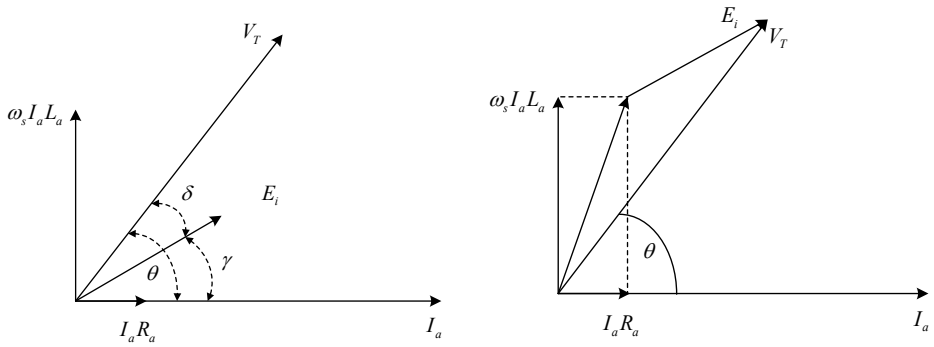

Figure 7. The phase diagrams of LSMs for each phase.

3. Proposed Sub-Sonic Linear Synchronous Motor Design Method

3.1. Design Guidelines

For the first step in the design of sub-sonic LSMs, the specifications of the pods should be determined in advance; those have been chosen, as shown in Table 1, considering the size of the sub-vacuum tubes and pods, on-board sub-systems, and driving profile schedules.

Table 1. Given requirements of sub-sonic pods and sub-vacuum tubes.

Parameter	Value	Unit
Total Mass of Pod, m_s	30,000	kg
Max. Acceleration, a_s	2	m/s^2
Length (Diameter) of Pod	35 (2)	m
Diameter of Sub-Vacuum Tubes	3.2	m
Passenger Seats	30	-

As shown in Figure 8, the 3D renderings reflect the final design model of the Hyperloop developed in KRRI and sub-systems such as HTS magnets with four poles–six modules and carbon-fiber monocoque chassis pods of 30,000 kg for 30 passenger seats.

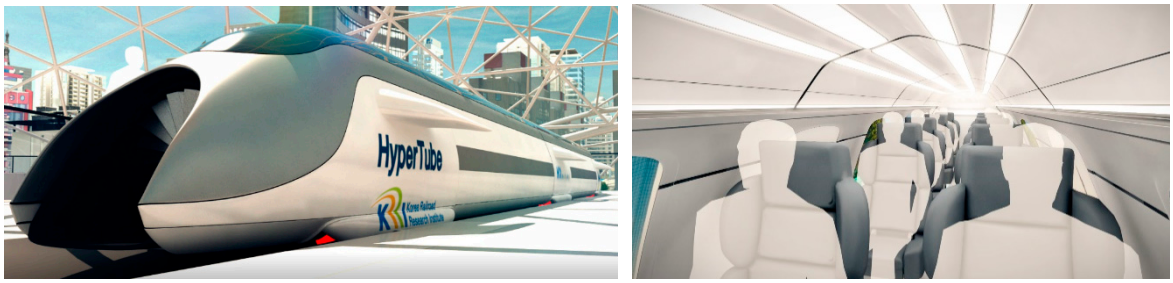

(**a**) (**b**)

Figure 8. Three-dimensional rendering of the pod of the Hyperloop: (**a**) outside; (**b**) inside.

After the design of the pods, in terms of the system engineering of the Hyperloop, HTS magnets represent a significant milestone since all the design parameters of HTS magnets are directly related to the design of armatures and PPSSs, which account for more than half of the total construction cost. Considering the technical limits of HTS magnets, armatures, and PPSSs, therefore, the specifications of HTS magnets have been chosen as shown in Table 2.

Table 2. Given requirements of HTS magnets adopting a four pole–six module system.

Parameter	Value	Unit
Magnetomotive Force of HTS Magnets, $N_f I_f$	750	kA·Turns
Number of Total Poles of HTS Magnets, P_e	24	-
Operating Temperatures	30	K
Air Gap, g	0.24	m
Pole Pitch, τ	2.7	M
Effective Length, l_f (Width, w_f)	2 (0.6)	m

Especially, the pole-pitch τ is a significant parameter for the design of inverters because the inverters suffer inevitable increases of their operating frequency f_s to double that in Equation (7) when the target sub-sonic velocity for the Hyperloop is twice the maximum speed of Maglev MLX with the same pole-pitch τ of 1.35 m [23]. This problem eventually leads to a doubled increase of the reactive power Q from (6b), which leads to an impractical manufacturing capacity and cost of armatures and inverters.

$$2\tau f_s = v_s \tag{7a}$$

$$f_s = \frac{v_s}{2\tau} \tag{7b}$$

$$\omega_s = 2\pi f_s \tag{7c}$$

At the same time, the magnetomotive force (MMF) $N_f I_f$ should be maximized within its technical limitations, as the product of $N_f I_f$ and $N_a I_a$ with given geometries of DC fields and armature windings is a constant for the required thrust forces in Equation (1). Similarly, a single power module of integrated gate-commutated thyristors (IGCTs), which can also provide a high-voltage (~10 kV) rating, guarantees stable operation with an inverter current I_a of 1000 A_{rms} under steady-states, and the current rating is considered to be the right current level for LSMs for the Hyperloop due to the inevitable conduction losses and cost of PPSSs.

$$L_a = N_p L_{pa} \cong N_p \frac{{N_a}^2}{\mathfrak{R}_{pa}} \tag{8a}$$

$$R_a = N_p R_{pa} \cong N_p \frac{\rho N_a l_a}{A_a} \tag{8b}$$

$$N_p = \frac{l_s}{\tau} \tag{8c}$$

However, when N_a and I_a are not high enough, this will lead to an unavoidable increase of N_a. From Equation (8a), it should be observed that L_a is directly proportional to the square of N_a while R_a is directly proportional to N_a. This problem also results in an enormous increase in the active power P, reactive power Q and manufacturing cost of armature windings, which is therefore far from the optimal design of LSMs, as it features poor efficiencies and power factors at sub-sonic speed operation. Here, l_s is the length of the armature section for each phase.

3.2. Design of Sub-Sonic Linear Synchronous Motors

For the design of the sub-sonic LSMs, the required thrust forces of the Hyperloop should be calculated, and this can be obtained from the required maximum acceleration of pods and resistance forces. As shown in Figure 9, aerodynamic F_a and electrodynamic F_d resistance forces are obtained by 3D simulation results, and it should be noted that F_a becomes an insignificant factor since pods are operated in a sub-vacuum tube of 0.001 atm.

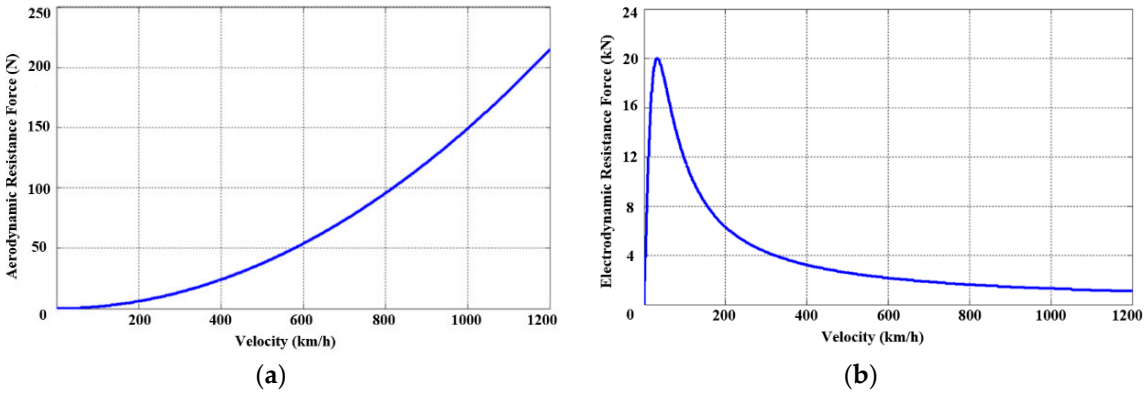

Figure 9. Simulation results of resistance forces for our Hyperloop model along with velocity: (**a**) aerodynamic resistance force; (**b**) electrodynamic resistance force with a g_c of 5 cm.

In addition, a_s is obtained assuming that EDS levitations using null-flux levitation coils [3] are adopted in the Hyperloop, which has been determined to be the best combination with LSMs using HTS magnets; therefore, F_d can also be variable in accordance with the selection of different levitation methods.

In practice, in order to reach the sub-sonic velocity of 1200 km/h in a short time, the initial target acceleration should be high enough while still being controlled below the limitation of 0.2 G (2 m/s^2); otherwise, the acceleration is likely to make passengers feel uncomfortable when it lasts for several minutes. In addition, for the efficient design of LSMPSs, as shown in Figure 10, there are two control regions—i.e., constant force and constant power regions—divided by the reference velocity of 600 km/h.

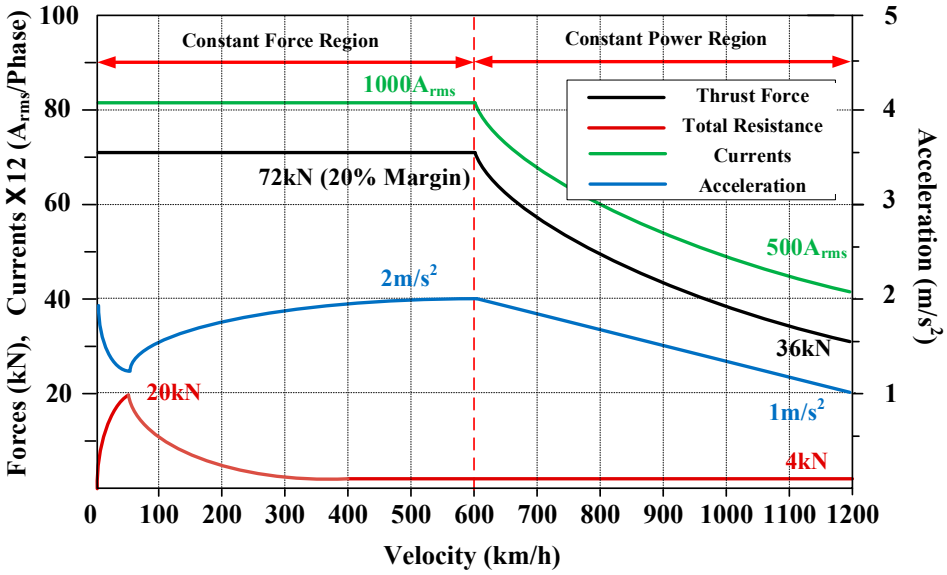

Figure 10. Profiles of forces, currents, and accelerations with proposed sub-sonic LSMs along with the velocity of pods.

In the constant force region, inverters flow constant currents into armature windings to generate constant forces on HTS magnets; on the other hand, in the constant power region, the currents and forces gradually decrease as the velocity linearly increases to maintain constant power. In fact, this is one of the most important design approaches to minimize the capacity of LSMs and VVVF inverters considering its practical design; therefore, the control method of the constant power region is essential for our Hyperloop application, even though longer distances are needed to reach its maximum operating speed.

Once the profiles with the two control regions are determined, as shown in Table 3, the design parameters of the proposed sub-sonic LSMs for the Hyperloop can be deducted from the design process addressed in Sections 2 and 3. In Table 3, it is found that the stator voltages and the minimum capacity of inverters show practical design specifications, which are similar stator voltages of 6 kV_{rms}/phase and half of theinverter capacity of 20 MVA [23] even at a sub-sonic velocity with respect to the JR-Maglev, MLX0.

Table 3. Design parameters of one-sided sub-sonic LSMs with HTS magnets adopting a four pole–six modules setup.

	Parameter	Value	Unit
DC Fields	Magnetomotive Force, $N_f I_f$	750	kA_{DC}·Turns
	Number of Total Poles, P_e	12	one-sided
	Pole Pitch, τ	2.7	m
	Air Gap, g	0.24	M
	Effective (Length l_f/Width w_f)	(2.25, 0.6)	m
Armatures	Phase Currents (600/1200 km/h), I_a	(1000/500)	A_{rms}
	Number of Coil Turns per Phase, N_a	2	Turns
	Magnetomotive Force (600/1200 km/h), $N_a I_a$	(2.8/1.4)	kA_{peak}·Turns
	Induced Voltages (600/1200 km/h], E_i	(2.7/5.4)	kV_{rms}/Phase
	Total Resistance per Section, R_a	0.59	Ω/Phase
	Total Inductance per Section, L_a	8.99	mH/Phase
	Effective (Length l_a/Width w_a)	(1.6/0.72)	m
	Cross Sectional Area of Litz-wire Conductors	300	mm^2/turn
Inverters	Stator Voltages (600/1200 km/h), V_T	(3.7/6.0)	kV/phase
	Frequency (600/1200 km/h), f_s	(31/62)	Hz
	Section Length	2	km
	Inverter Capacity (600/1200 km/h)	(11/9)	MVA

4. Experimental Verifications

In order to verify the proposed design models of the sub-sonic LSMs, two experimental sets of LSMs with a two pole–one module HTS magnet and two pole–two module electromagnets, respectively, were fabricated for the static and dynamic tests, as shown in Figure 11. Two different test-beds—i.e., static and dynamic propulsion test-beds—should be fabricated in general since it is difficult to verify the characteristics of generated forces between the DC field and armature windings while a pod is moving on guideways.

Due to the limitations of budget and time, the experimental parameters of sub-sonic LSMs in the two test-beds are different from the final design in Table 3; however, it should be noted that it is worthwhile to verify proposed design methods with experimental and simulation results.

4.1. Static Propulsion Tests

In order to conduct the static propulsion test, the reference point at which one of the three-phase currents reaches zero and the others have the same magnitudes of currents, as shown in Figure 12, is selected to validate the characteristics of the generated forces in a time-invariant state.

At the reference point, the experiment sets could therefore be more simplified as inverters can be replaced with DC power supply systems, as shown in Figure 13, which is able to flow I_a of 300 A_{DC} into armature windings; the experimental parameters of the static propulsion test are summarized in Table 4.

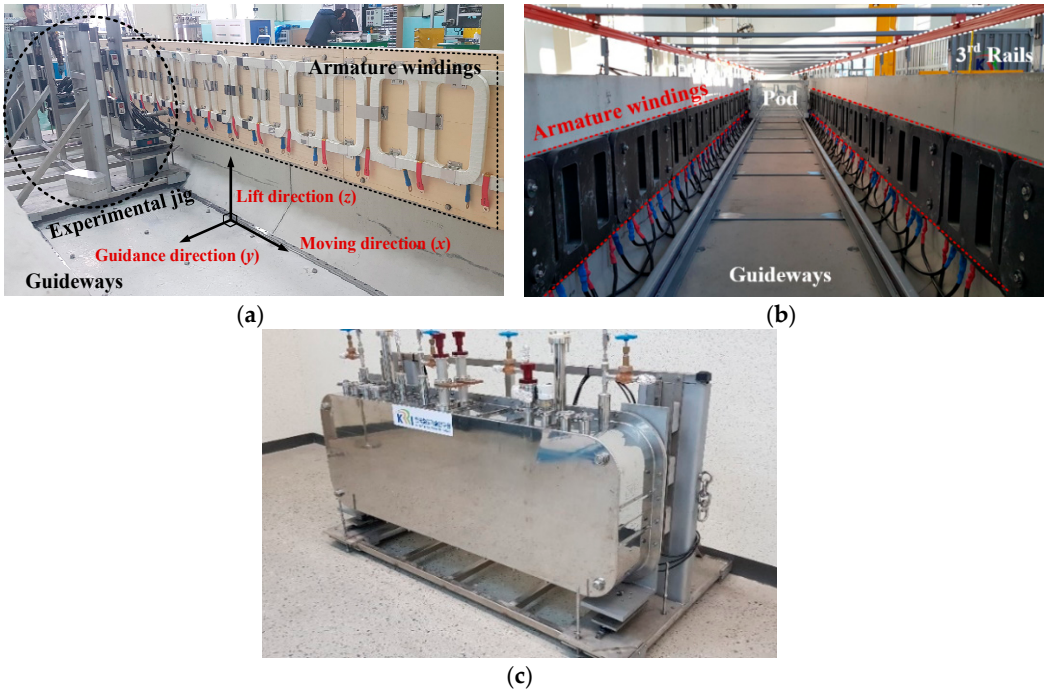

(**a**) (**b**)

(**c**)

Figure 11. Two experimental sets of the sub-sonic LSMs: (**a**) 6 m long static propulsion test-bed; (**b**) 20 m long dynamic propulsion test bed; (**c**) fabricated HTS magnet for the static test.

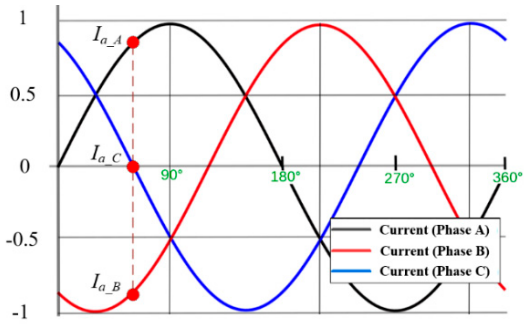

Figure 12. Diagram of three-phase currents—i.e., the current of phase A I_{a_A}, B I_{a_B}, and C I_{a_C}—showing the reference point at which one of three-phase currents reaches zero and the others have the same magnitudes of currents.

(**a**) (**b**)

Figure 13. Experimental sets of the LSMs for the static propulsion test: (**a**) test-bed with the HTS magnet installed on the experimental jig; (**b**) one of the four mechanical stoppers on linear guide rails.

Table 4. Experimental parameters of the static propulsion test of one-sided LSMs with HTS magnets adopting a two pole–one module setup.

	Parameter	Value	Unit
DC Fields	Magnetomotive Force, $N_f I_f$	150	kA_{DC}·Turns
	Operating Current, I_{op}	84	A_{DC}
	Total Number of Coil, N_f	1784	Turns
	Number of Total Poles, p_e	2	one-sided
	Operating Temperature	<40	K
	Cooling Method	Conductive Colling	-
	Tape Material (SuNAM Co.)	GdBCO	-
	Pole Pitch, τ	0.81	m
	Air Gap, g	0.17	m
	Effective (Length l_f/Width w_f)	(0.6, 0.3)	m
	Inductance	5.2	H
Armatures	Phase Currents, I_a	300	A_{DC}
	Number of Coil Turns per Phase, N_a	11	Turns
	Magnetomotive Force, $N_a I_a$	3300	A_{DC}·Turns
	Effective (Length l_a/Width w_a)	(0.46/0.32)	m
	Cross Sectional Area of Al Conductors	80	mm^2/turn

As shown in Figures 11a and 13a, seven load-cells (BONGSHIN, DSCK) are adopted in the experimental jig, which is designed for the installation of the two pole–one module HTS magnet, to measure three-axis forces on the HTS magnet while the experimental jig is only able to move to the x-axis (thrust force direction) in order to set the variable δ of one-sided armature windings for the static test. After the experimental jig is located in assigned measurement points of thrust forces, as shown in Figure 13b, the freedom of the minus x-axis is restricted by stoppers to measure thrust forces for safety issues.

The thrust, guidance, and lift forces for different δ values were measured and compared with the simulation results, as shown in Figure 14. As expected from the thrust and guidance force models of Equation (2) and previous simulation results of Figure 5, the thrust and guidance forces are perfectly symmetric with respect to the power angle of 90° and the life forces are zero, as the center to center of the z-axis (lift direction) for both HTS magnets and armature windings are well aligned.

In general, theoretical, simulation and experimental results are well matched to each other except for the measured thrust forces at the power angles of 15° and 165°. This is because the generated thrust forces are smaller than the maximum static friction force of about 200 N for the experimental jig; therefore, the measured thrust forces of the x-axis load-cell indicate zero. In order to solve these issues, maximum static friction forces for each measurement point are measured by the x-axis load-cell and added to the measured thrust forces.

4.2. Dynamic Propulsion Tests

For the dynamic propulsion test, double-sided armature windings are installed on both sides of the guideway in the dynamic test-bed and are modularized with epoxy molding compounds to endure dynamic forces and obtain a lower construction cost and time, as shown in Figures 11b and 15a. In addition, the sub-sonic LiDAR system, which has a measurement resolution of 3 cm and sampling time of 20 ms, is adopted for the synchronization between DC fields and armature windings.

In order to verify the dynamic propulsion test, a small-scaled experimental pod was fabricated and the experimental requirements are summarized in Table 5. Here, the pod includes two pole–one module electromagnets for each side, and third rails and pick-ups are installed on the guideway and pod, respectively, to supply required currents from a DC power supply into moving electromagnets on the pod.

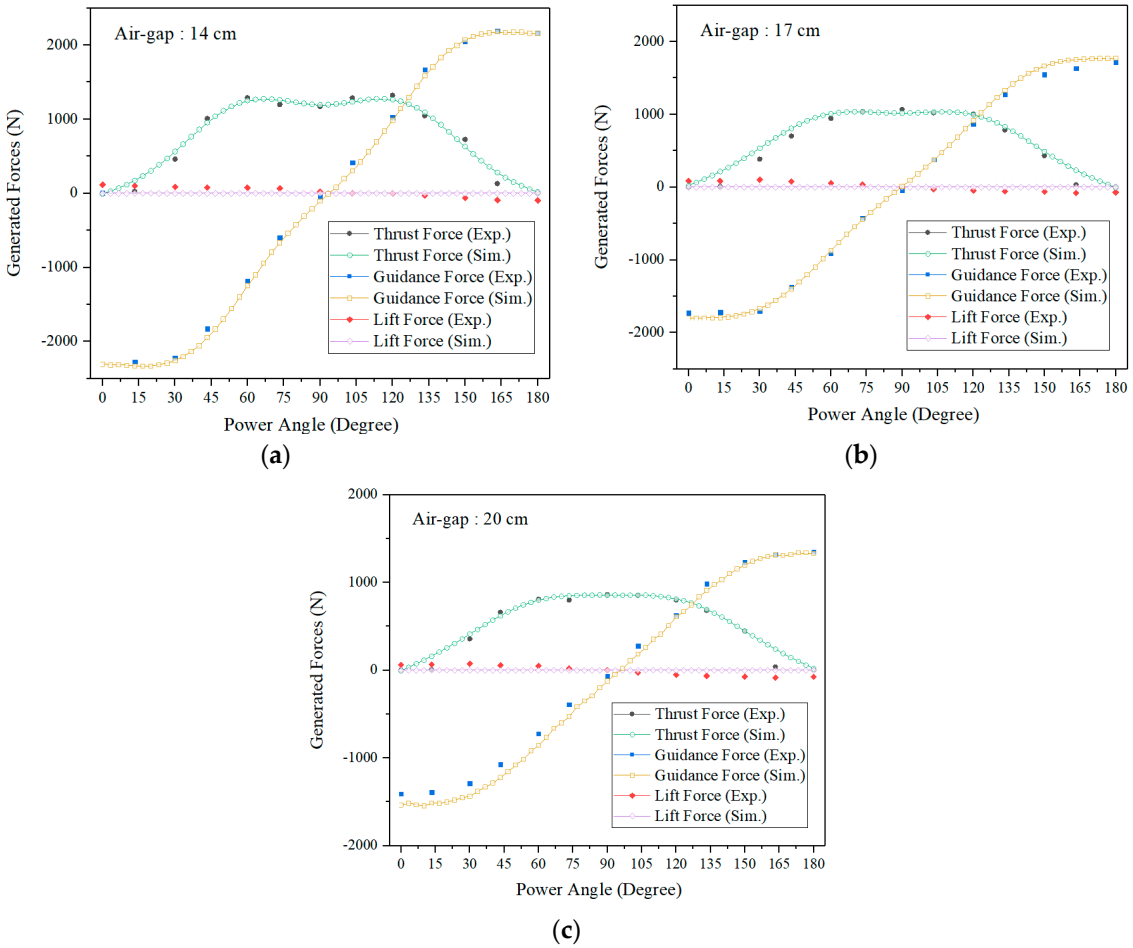

Figure 14. Experimental and 3D simulation (Infolytica, MagNet) results of generated forces along with variable power angles with g_c of 0 for the static propulsion test: (**a**) air-gap of 14 cm, (**b**) 17 cm, (**c**) and 20 cm.

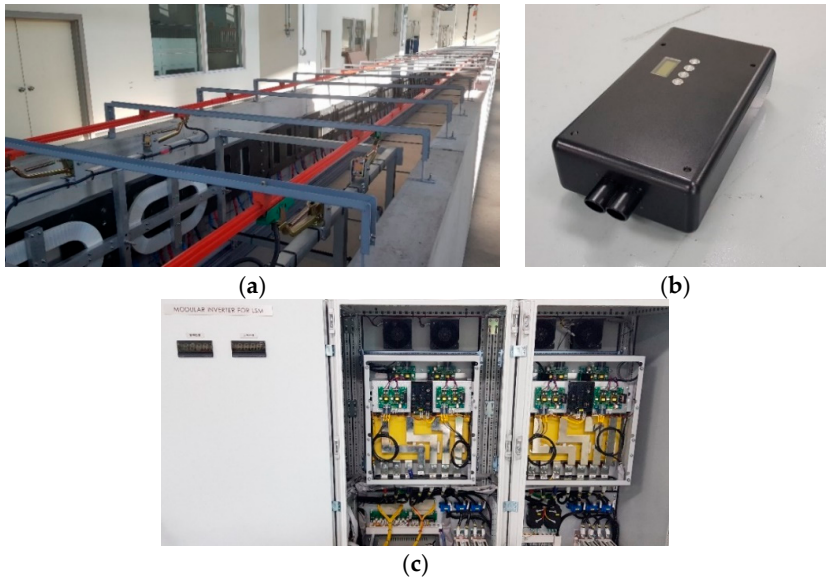

Figure 15. Experimental sets of the LSMs for the dynamic propulsion test: (**a**) dynamic test-bed with a pod with two pole–two module electromagnets; (**b**) sub-sonic LiDAR system for the precision non-contact location measurement of a pod; (**c**) modular inverters for LSMs.

Table 5. Given requirements of the dynamic propulsion test with a small-scaled pod.

Parameter	Value	Unit
Total Mass of Pod, m_s	100	kg
Max. Acceleration, a_s	1	m/s^2
Max. Velocity, v_s	3(10)	m (km/h)
Length of Pod	1.5	m
Length of Test-bed	20	m

After the requirements are established, as shown in Table 6, main parameters for the dynamic propulsion test can be determined in accordance with the design methods of Sections 2 and 3. Here, double-sided armature modules are connected in series due to the short test-bed of 20 m, and the air gap g is minimized to maximize the acceleration and velocity of the pod.

Table 6. Designed parameters of the dynamic propulsion test of double-sided LSMs with electromagnets adopting a two pole–two module setup.

	Parameter	Value	Unit
DC Fields	Magnetomotive Force, $N_f I_f$	6	kA$_{DC}$·Turns
	Number of Total Poles, p_e	4	one-sided
	Pole Pitch, τ	0.81	m
	Air Gap, g	0.07	m
	Effective (Length l_f/Width w_f)	(0.6, 0.3)	m
Armatures	Phase Currents, I_a	300	A$_{DC}$
	Number of Coil Turns per Phase, N_a	11	Turns
	Magnetomotive Force, $N_a I_a$	3300	A$_{DC}$·Turns
	Induced Voltages [10 km/h], E_i	1	V$_{rms}$/Phase
	Total Resistance per Section, R_a	0.35	Ω/Phase
	Total Inductance per Section, L_a	6.35	mH/Phase
	Effective (Length l_a/Width w_a)	(0.46/0.32)	M
	Cross Sectional Area of Al Conductors	80	mm^2/turn
Inverters	Stator Voltages (10 km/h), V_T	37	V$_{rms}$/phase
	Frequency (10 km/h), f_s	1.85	Hz
	Section Length	40	m
	Required Inverter Capacity	15	kVA

Since the sum of measured friction forces from the wheels and pick-ups of the pod is nearly 20 N, the averaged thrust force for 120 N is designed to meet the maximum acceleration of 1 m/s^2. As shown in Figure 16, the experimental results from the control data of modular inverters for LSMs show excellent agreement with the requirements and designed parameters in Tables 5 and 6, which are determined from proposed design methods.

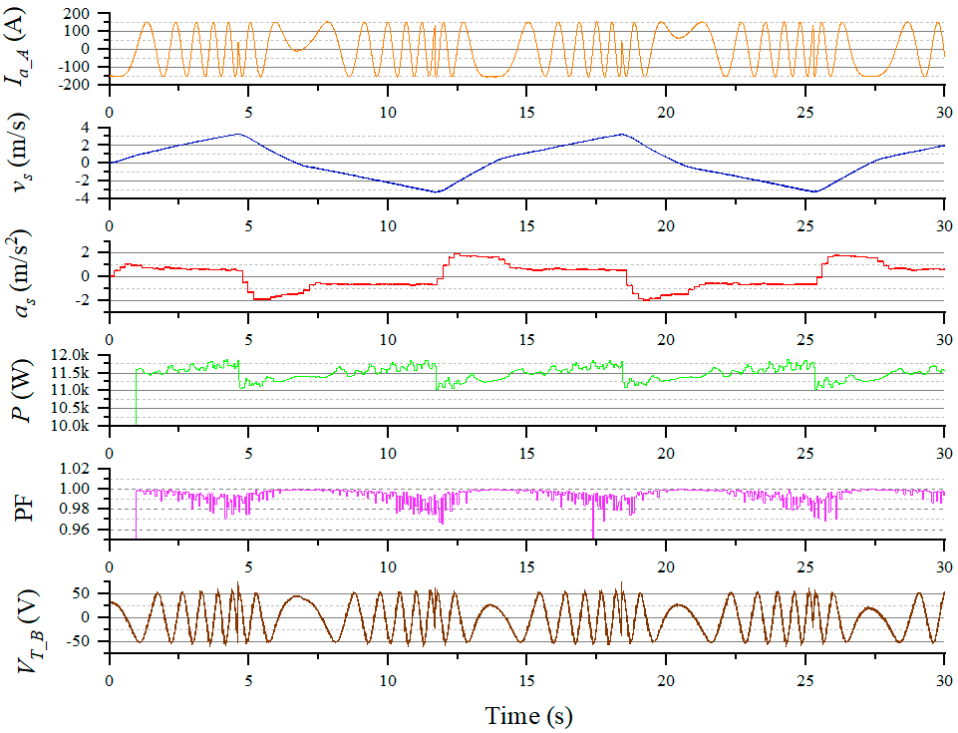

Figure 16. Experimental results of the dynamic propulsion test with a small-scaled pod.

5. Conclusions

In this paper, the characteristics of proposed LSMs with HTS magnets are widely analyzed using the theories as well as simulation results, and optimal design methods for armatures and inverters in terms of the system engineering are newly introduced with the design guidelines and examples for a commercialized version of the Hyperloop. By virtue of the combination of LSMs and electrodynamic suspensions (EDSs) with HTS magnets, a large air-gap of 24 cm, low magnetic resistance forces of below 2 kN, and an efficient as well as practical design of propulsion power supply systems of around 10 MVA could be guaranteed at a sub-sonic velocity. In the experimental verification with two different test-beds—i.e., 6 m long static and 20 m long dynamic propulsion test-beds—it was found that the proposed design models of the sub-sonic LSMs with HTS magnets were well matched with simulation and experimental results under minor numerical errors of 5% in the static and dynamic propulsion tests; therefore, it can be said that proposed design methods and experimental approaches could be guidelines for those aiming to design sub-sonic LSMs for a Hyperloop.

Author Contributions: Conceptualization, S.Y.C. and C.Y.L.; methodology, S.Y.C. and J.Y.L.; software, S.Y.C. and J.Y.L.; validation, J.H.C. and Y.J.O.; formal analysis, J.M.J.; writing—original draft preparation, S.Y.C; writing—review and editing, S.Y.C.; visualization, S.Y.C.; supervision, C.Y.L.; project administration, C.Y.L.; funding acquisition, K.S.L.

Funding: This research was supported by a grant from the R&D program of the Korea Railroad Research Institute, Republic of Korea with the project entitled "Core Technology Development of Subsonic Capsule Train (Hyper Tube Express, HTX)."

Acknowledgments: Su Y. Choi would like to acknowledge the support of the following organizations: Korea National University of Transportation, Changwon National University and SuperGenics in South Korea.

Conflicts of Interest: The authors declare no conflict of interest. The funders had no role in the design of the study; in the collection, analyses, or interpretation of data; in the writing of the manuscript, or in the decision to publish the results.

Nomenclature

F_{max}	Generated maximum force.
F_t	Thrust force.
F_g	Guidance force.
F_m	Mechanical force.
F_r	Total resistance force.
F_f	Effective thrust force.
F_a	Aerodynamic resistance force.
F_d	Electrodynamic resistance force.
F_i	Incline resistance force.
c	Design constant including geometric factor.
μ_o	Absolute permeability of vacuum.
m_a	Number of phases.
p_e	Number of field pole pairs.
τ	Pole pitch.
α	Air-gap constant.
g	Air-gap in x-axis.
g_c	Air-gap in z-axis.
l_a	Effective length of armature winding.
l_f	Effective length of field winding.
w_a	Effective width of armature winding.
w_f	Effective width of field winding.
N_a	Number of coil turns for armatures.
N_f	Number of coil turns for DC fields.
I_a	Current of armature windings.
I_f	Current of field windings.
δ	Power angle.
V_T	Stator voltage for each phase.
R_a	Resistance of armatures for each phase.
L_a	Inductance of armatures for each phase.
N_p	Number of armature poles for each phase
R_{pa}	Resistance of each pole of armatures.
L_{pa}	Inductance of each pole of armatures.
E_i	Induced voltage of armatures per phase.
c_i	Induced voltage constant.
v_s	Speed of pods.
m_s	Mass of pods.
a_s	Acceleration of pods.
P_e	Electrical power.
P_m	Mechanical power.
P	Active power.
Q	Reactive power.
S	Complex power.
γ	Phase difference between E_i and I_a.
l_s	Length of the armature section per phase.
f_s	Operating frequency.
ϕ_a	Magnetic fluxes passing through armature.

References

1. Abdelrahman, A.S.; Youssef, M.Z. Hyperloop Transportation System: Analysis, Design, Control, and Implementation. *IEEE Trans. Ind. Electron.* **2018**, *65*, 7427–7436. [CrossRef]
2. Palacin, R. Hyperloop, the Electrification of Mobility, and the Future of Rail Travel. *IEEE Electrif. Mag.* **2016**, *4*, 4–51. [CrossRef]

3. Lee, H.W.; Kim, K.C.; Lee, J. Review of maglev train technologies. *IEEE Trans. Magn.* **2006**, *42*, 1917–1925.
4. Lee, H.W.; Park, C.B.; Lee, J. Improvement of thrust force properties of linear synchronous motor for an ultra-high-speed tube train. *IEEE Trans. Magn.* **2011**, *47*, 4629–4634. [CrossRef]
5. Bohn, G.; Steinmetz, G. The electromagnetic levitation and guidance technology of the Transrapid test facility Emsland. *IEEE Trans. Magn.* **1984**, *20*, 1666–1671. [CrossRef]
6. Yamamura, S. Magnetic levitation technology of tracked vehicles present status and prospects. *IEEE Trans. Magn.* **1976**, *12*, 874–878. [CrossRef]
7. Shinha, P. Design of a magnetically levitated vehicle. *IEEE Trans. Magn.* **1984**, *20*, 1672–1674. [CrossRef]
8. Rogg, D. General survey of the possible applications and development tendencies of magnetic levitation technology. *IEEE Trans. Magn.* **1984**, *20*, 1696–1701. [CrossRef]
9. Fujimoto, T.; Aiba, M.; Suzuki, H.; Umeki, T.; Nakamura, S. Characteristics of electromagnetic force of ground coil for levitation and guidance at the Yamanashi Maglev test line. *Q. Rep. Rtri* **2000**, *41*, 63–67. [CrossRef]
10. Space X Website. Available online: https://www.spacex.com/sites/spacex/files/hyperloop_alpha-20130812.pdf (accessed on 25 November 2019).
11. Mossi, M.; Rossel, P. Swissmetro: A revolution in the high speed passenger transport systems. In Proceedings of the1st Transport Research Conference, Ascona, Switzerland, 1–3 March 2001; pp. 1–16.
12. Lee, H.W.; Cho, S.Y.; Cho, W.Y.; Lee, J.; Kwon, H.B. Analysis of the magnetic effect on the tube infrastructure for a super speed tube train. *Int. J. Railw.* **2009**, *2*, 170–174.
13. Korea Railroad Research Institute. *Development of Core Technologies of Ultra-High-Speed Tube Train Project*; Korea Railroad Research Institute Internal Report; Korea Railroad Research Institute: Gyeonggi-do, Korea, 2009.
14. Virgin Hyperloop One Website. Available online: https://hyperloop-one.com/ (accessed on 25 November 2019).
15. Hyperloop Transportation Technologies (HTT) Website. Available online: https://www.hyperloop.global/ (accessed on 25 November 2019).
16. Official YouTube of Virgin Hyperloop One. Available online: http://bitly.kr/BiyXut1 (accessed on 25 November 2019).
17. Official YouTube of Hyperloop Transportation Technologies (HTT). Available online: https://c11.kr/9y2n (accessed on 25 November 2019).
18. Ji, W.Y.; Jeong, G.; Park, C.B.; Jo, I.H.; Lee, H.W. A study of non-symmetric double-sided linear induction motor for Hyperloop all-in-one system (propulsion, levitation, and guidance). *IEEE Trans. Magn.* **2018**, *54*, 1–4. [CrossRef]
19. Cho, H.W.; Sung, H.K.; Sung, S.Y.; You, D.J.; Jang, S.M. Design and characteristic analysis on the short-stator linear synchronous motor for high-speed maglev propulsion. *IEEE Trans. Magn.* **2008**, *44*, 4369–4372.
20. Lee, C.Y.; Lee, J.H.; Lee, J. Conceptual design of superconducting linear synchronous motor for 600-km/h wheel-type railway. *IEEE Trans. Appl. Supercond.* **2014**, *24*, 1–4. [CrossRef]
21. Gong, T.; Ma, G.; Qian, H.; Zhang, W. Electromagnetic investigation of a high-temperature superconducting linear synchronous motor for high-speed railway. *IEEE Trans. Appl. Supercond.* **2018**, *28*, 1–5. [CrossRef]
22. Park, C.B.; Lee, B.S.; Lee, C.Y. Characteristic analysis of superconducting LSM for the wheel-rail-guided very high speed train according to winding method of the ground 3-phase coils. *Trans. Korean Inst. Electr. Eng.* **2014**, *63*, 1164–1169. [CrossRef]
23. Li, J.; Yen, F.; Zheng, S.; Wang, S.; Wang, J. Normal force analysis on a high temperature superconducting linear synchronous motor. *IEEE Trans. Appl. Supercond.* **2012**, *22*, 5200304.
24. Zheng, L.; Jin, J.; Guo, Y.; Xu, W.; Zhu, J. Performance analysis of an HTS magnetic suspension and propulsion system with a double-sided HTS linear synchronous motor. *IEEE Trans. Magn.* **2012**, *48*, 655–658. [CrossRef]
25. Zheng, S.J.; Yen, F.; Wang, S.Y. Performance of a small –scale high temperature superconducting linear synchronous motor prototype. *IEEE Trans. Appl. Supercond.* **2012**, *22*, 5200104. [CrossRef]
26. Gieras, J.F.; Piech, Z.J. *Linear Synchronous Motors: Transportation and Automation Systems*; CRC Press: Boca Raton, FL, USA, 1999.